Enhanced Photocatalytic Performances of CeO₂/TiO₂ Nanobelt Heterostructures

Jian Tian, Yuanhua Sang, Zhenhuan Zhao, Weijia Zhou, Dongzhou Wang, Xueliang Kang, Hong Liu,* Jiyang Wang, Shaowei Chen,* Huaqiang Cai, and Hui Huang

CeO₂/TiO₂ nanobelt heterostructures are synthesized via a cost-effective hydrothermal method. The as-prepared nanocomposites consist of CeO₂ nanoparticles assembled on the rough surface of TiO₂ nanobelts. In comparison with P25 TiO₂ colloids, surface-coarsened TiO₂ nanobelts, and CeO₂ nanoparticles, the CeO₂/TiO₂ nanobelt heterostructures exhibit a markedly enhanced photocatalytic activity in the degradation of organic pollutants such as methyl orange (MO) under either UV or visible light irradiation. The enhanced photocatalytic performance is attributed to a novel capture–photodegradation–release mechanism. During the photocatalytic process, MO molecules are captured by CeO₂ nanoparticles, degraded by photogenerated free radicals, and then released to the solution. With its high degradation efficiency, broad active light wavelength, and good stability, the CeO₂/TiO₂ nanobelt heterostructures represent a new effective photocatalyst that is low-cost, recyclable, and will have wide application in photodegradation of various organic pollutants. The new capture–photodegradation–release mechanism for improved photocatalysis properties is of importance in the rational design and synthesis of new photocatalysts.

J. Tian, Dr. Y. Sang, Z. Zhao, Dr. W. Zhou, D. Wang,
X. Kang, Prof. H. Liu, Prof. J. Wang, Prof. S. Chen
State Key Laboratory of Crystal materials
Center of Bio & Micro/nano Functional Materials
Shandong University
Jinan, 250100, PR China
E-mail: hongliu@sdu.edu.cn; shaowei@ucsc.edu

Prof. H. Liu
Beijing Institute of Nanoenergy and Nanosystems
Chinese Academy of Science
Beijing, 100864, PR China

Prof. S. Chen
Department of Chemistry and Biochemistry
University of California
1156 High Street, Santa Cruz, California, 95064, USA

Dr. H. Cai, Prof. H. Huang
Institute of Chemical Materials
China Academy of Physical engineering
Mianyang, 621900, PR China

1. Introduction

One-dimensional nanostructures, such as nanowires, nanotubes, nanorods and nanobelts, have received a great deal of attention during the last decade due to their dimensional confinement and unique structurally well-defined physical and chemical properties.[1,2] Among these, numerous approaches have been developed to prepare one-dimensional TiO₂ nanostructures, such as TiO₂ nanobelts, because of their low number of grain boundaries, fast charge transfer dynamics and high specific surface area, which can improve the photocatalytic performance.[3] However, there are two bottlenecks which hinder the applications of TiO₂ nanobelts as photocatalysts. One is the high recombination rate of the photoinduced electron-hole pairs because of the single-phase nanobelt structure,[4] and the other is that pure TiO₂ can only absorb ultraviolet light, which accounts for only about 4% of the sunlight, due to its large bandgap (3.2 eV for anatase, and 3.0 eV for rutile), and hence prevents its widespread applications.[5] To solve these problems, a number of

strategies have been reported to reduce the charge recombination and enhance visible light utilization of TiO_2 nanobelts. For instance, Zhou et al. prepared TiO_2 nanoparticles/TiO_2 nanobelts by an acid-assisted hydrothermal method which exhibited enhanced photocatalytic activity.[6] Another cost-effective alternative is to couple TiO_2 nanobelts with other semiconductors, metals, and conductive macromolecules to form heterostructures. Based on band matching and interface engineering, the TiO_2 nanobelts-based nanoheterostructure promote the separation of photoinduced electron-hole pairs by the effective transfer of photogenerated electrons and holes at the interface.[7] Furthermore, interfacial engineering with the attachment of visibly active photocatalytic nanoparticles on the TiO_2 nanobelt surface has been found to lead to marked enhancement of the photocatalytic activity in both the UV and visible regions.[8]

As a nontoxic and inexpensive rare earth material, ceria (CeO_2) has attracted extensive attention in catalysis.[9,10] For instance, Borker et al. discussed the photocatalytic behaviors of CeO_2 under sunlight irradiation in the degradation of organic dyes.[11] In some other studies, the excellent photocatalytic ability of CeO_2/TiO_2 nanocomposite materials has been examined.[12] For example, Li et al. reported that the introduction of CeO_2 into the TiO_2 framework not only improved the thermal stability of the ordered mesoporous structure, but also effectively extended the photo-response of TiO_2 to the visible light region.[13] In this study, we present a new strategy whereby CeO_2 nanoparticles were assembled onto the TiO_2 nanobelt surface and the resulting heterostructures exhibited substantial enhancement of the photocatalytic activity in the degradation of organic pollutants by using MO as the illustrating example.

In this work, CeO_2/TiO_2 nanobelt heterostructures were synthesized through a low cost hydrothermal-co-precipitation method. The band matching of the nanoheterostructures effectively suppressed the rate of hole-electron recombination and improved the photocatalytic activity that was apparent in the UV and visible range. This was accounted for by a capture-degradation-release mechanism, which may be of fundamental significance in the rational design and synthesis of highly effective photocatalysts by interfacial engineering.

2. Results and Discussion

The structures of the nanobelt samples were first characterized by X-ray powder diffraction (XRD) measurements. **Figure 1** depicts the XRD patterns of TiO_2 nanobelts, CeO_2 nanoparticles and CeO_2/TiO_2 nanobelt heterostructures. In curve (a), the diffraction peaks at $2\theta = 25.28°$, $37.80°$, $48.05°$, $53.89°$, $55.06°$, and $62.69°$ are assigned to anatase TiO_2 (PDF-#21-1272). For pure CeO_2 nanoparticles (curve b), the peaks at $2\theta = 28.68°$, $33.28°$, $47.84°$, $56.78°$, and $59.60°$ are attributed to the (111), (200), (220), (311) and (222) faces of cubic CeO_2 (PDF-#34-0394), respectively. For CeO_2/TiO_2 nanobelt heterostructures (curve c), all the diffraction peaks can be well indexed to either TiO_2 or CeO_2. The broad diffraction peaks of CeO_2 can be attributed to the small grain size of
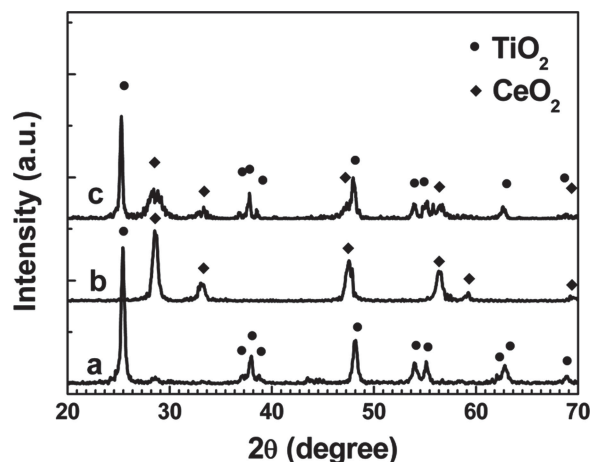

Figure 1. XRD patterns of (a) TiO_2 nanobelts, (b) CeO_2 nanoparticles, and (c) CeO_2/TiO_2 (mole ratio 2:10) nanobelt heterostructures.

CeO_2 nanoparticles on the surface of TiO_2 nanobelts.[14] The X-ray photoelectron spectroscopy (XPS) of pure CeO_2 nanoparticles (Figure S1a, in Supporting Information (SI)) shows that only the characteristic peaks attributed to Ce^{4+} were observed. In CeO_2/TiO_2 nanobelt heterostructures, the peaks attributed to Ce^{4+} were still predominant. However, as shown in Figure S1b, the small peaks of v1and u1 belonging to Ce^{3+} were detected. No peaks from other phases, except for TiO_2 and CeO_2, were detected in Figure S1c, thereby indicating that Ce^{3+} compound might be amorphous or too little to be checked out.

The morphology and microstructure of the samples were then examined by scanning electron microscopy (SEM) and high-resolution transmission electron microscopy (HRTEM) measurements. **Figure 2** shows the SEM images of (a) TiO_2 nanobelts, (b) CeO_2 nanoparticles, and (c) CeO_2/TiO_2 nanobelt heterostructures. It can be seen that the TiO_2 nanobelts are 50–200 nm in width and 20–40 nm in thickness (Figure 2a). The length of the nanobelts can range up to tens of micrometers. The surface of the TiO_2 nanobelts is very coarse, exhibiting a large specific surface area. The CeO_2 nanoparticles (Figure 2b) synthesized by the hydrothermal-co-precipitation method are homogeneous in size of about 20 nm. It is likely that with the high specific surface area of the CeO_2 nanoparticles come a large number of dangling bonds (metal-oxygen, M-O and oxygen-hydrogen, O-H) on the nanoparticle surface that may facilitate the adsorption of pollutant molecules.[15] As is shown in Figure 2c, the SEM image of CeO_2/TiO_2 nanobelt heterostructures shows that the CeO_2 nanoparticles were well dispersed on the surface of the TiO_2 nanobelts. The surface-coarsened TiO_2 nanobelts provide numerous nucleation sites for the growth of CeO_2 nanoparticles, leading to the formation of homogeneously dispersed CeO_2 nanoparticles on the TiO_2 nanobelt surface. Energy-dispersive X-ray spectroscopy (EDS) analysis (Figure 2d) confirmed that the CeO_2/TiO_2 nanobelt heterostructures are composed of Ti, Ce, and O.

The structures of the nanobelt composites were further investigated by HRTEM measurements, as manifested in
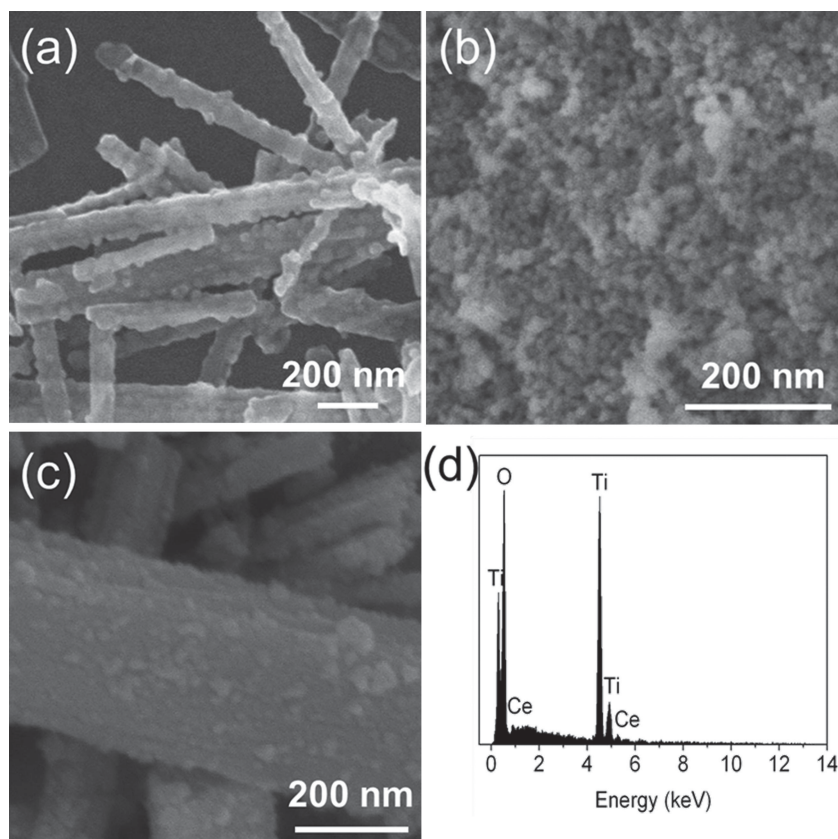
Figure 2. Typical SEM images of (a) TiO_2 nanobelts, (b) CeO_2 nanoparticles, (c) CeO_2/TiO_2 (mole ratio 2:10) nanobelt heterostructures, (d) energy-dispersive X-ray spectroscopy of the CeO_2/TiO_2 (mole ratio 2:10) nanobelt heterostructures. Scale bars in (a–c) are all 200 nm.

before irradiation. Interestingly, the CeO_2/TiO_2 heterostructures exhibited apparent photocatalytic activity even under visible light irradiation, whereas the TiO_2 nanobelts alone were photocatalytically active only in the UV range. As shown in panel (a), after 25 min of visible light irradiation, 87% of MO was photodegraded by the CeO_2/TiO_2 (mole ratio 2:10) nanobelt heterostructures, whereas 60% by CeO_2 nanoparticles. These performances are much better than that of TiO_2 nanobelts alone (17%), which is comparable to that of P25 TiO_2 colloids (20%). Note that the degradation of MO in the absence of a catalyst under visible light irradiation is negligible (Figure S2). Similar behaviors were observed under UV light irradiation, as manifested in panel (b). Again, after 25 min of UV irradiation, nearly 100% of MO was degraded with the CeO_2/TiO_2 (2:10) nanobelt heterostructures, which was significantly better than those of P25 TiO_2 colloids (65%), TiO_2 nanobelts (62.3%), and CeO_2 nanoparticles (25.1%). Moreover, the value of $(1-C/C_0)$ of MO is 25.9% while the CeO_2/TiO_2 nanobelt heterostructures are kept in the dark for the same time (Figure S2), which is much less than 87%, owing to the capture of MO on the catalysts, which will be confirmed by the FTIR spectra in the below. All these

measurements show that the CeO_2/TiO_2 nanobelt heterostructures exhibited much enhanced photocatalytic activity as compared to the TiO_2 nanobelts or CeO_2 nanoparticles alone, although the capture of MO can occur before photocatalysis process. The excellent photocatalytic degradation of MO under UV and visible light irradiation can be attributed to the large specific area of the CeO_2/TiO_2 nanobelt heterostructures (Table S1 in the SI). The BET specific surface area of the TiO_2 nanobelt is 32.229 m^2 g^{-1}, while the value of the acid corroded TiO_2 nanobelt increases to 38.591 m^2 g^{-1}. Surprisingly, the CeO_2/TiO_2 nanobelt heterostructure displays a larger specific surface area (122.507 m^2 g^{-1}) than those of CeO_2 nanoparticles (61.577 m^2 g^{-1}) and TiO_2 nanobelts alone, which leads to the exposure of more active sites and hence higher photocatalytic activity.

It is worth noting that the absorption of MO for CeO_2/TiO_2 nanobelt heterostructures in the dark is higher than that for other photocatalysts, which can be attributed to the heterostructure's higher capture capacity (Figure S3). In addition, we have found that when CeO_2/TiO_2 nanobelt heterostructures were dispersed in MO solution and kept in the dark for 30 min, the catalyst powders become orange (Figure S4b), and change back to light yellow, the original color of CeO_2/TiO_2 nanobelt heterostructures, after irradiation of UV or visible light for 30 min (Figure S4c) on these orange photocatalyst. This phenomenon implies that MO can be easily captured by CeO_2/TiO_2 nanobelt heterostructures,
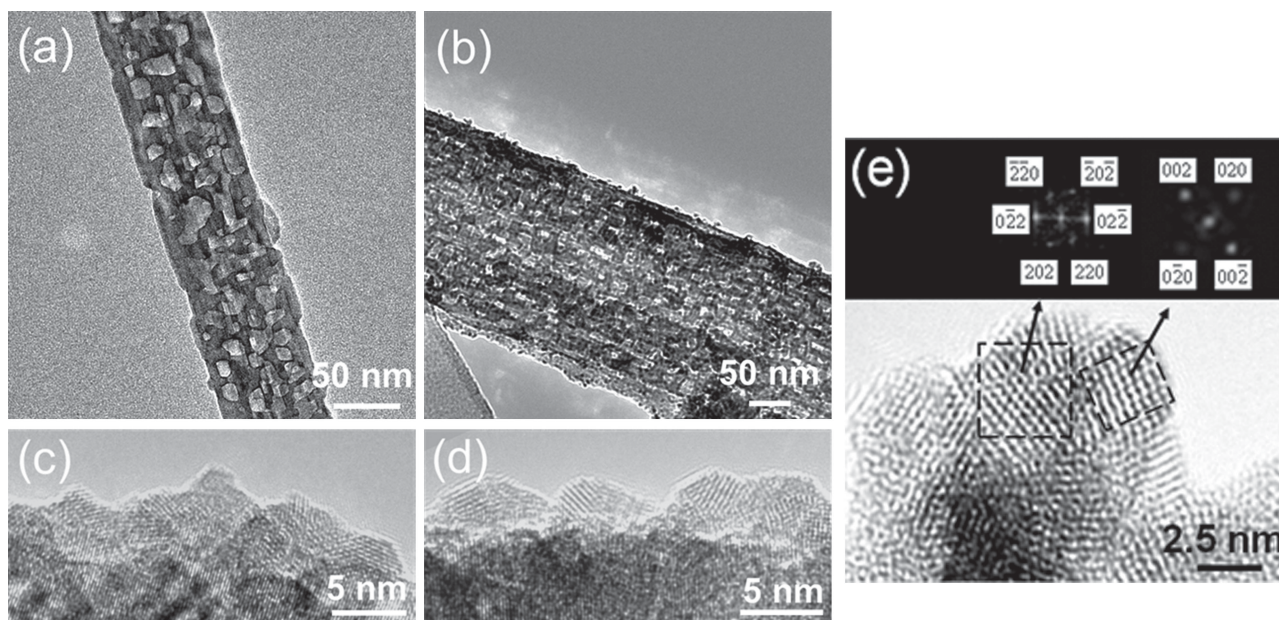
Figure 3. It can be seen that surface morphologies of the as-prepared surface-coarsened TiO_2 nanobelts (Figure 3a) and the CeO_2/TiO_2 nanobelt heterostructures (Figure 3b) were very consistent. Nonetheless, a large number of CeO_2 nanoparticles can be seen to distribute rather uniformly on the TiO_2 nanobelt surface (Figure 3b). In Figure 3c and d, high-resolution measurements showed that a layer of CeO_2 nanoparticles of about 5 nm in diameter were intimately attached on the surface of TiO_2 nanobelts leading to the formation of nanoheterostructures, as revealed by the SEM measurements (Figure 2). Figure 3e shows the lattice images of the nanoparticles with special 2-dimensional fringes, including square lattice points and hexagonal lattice point. Fourier-transform electron diffraction patterns (inset to Figure 3e) further demonstrate the square lattice and hexagonal lattice images of the cubic CeO_2 nanoparticles.[16] The combined XRD and EDS results show that the nanoheterostructures were indeed formed by the attachment of CeO_2 nanoparticles onto the TiO_2 nanobelt surface, which may improve the efficiency of interfacial charge separation and hence the photocatalytic activity.

To investigate the photocatalytic activity of the CeO_2/TiO_2 nanobelt heterostructures, the degradation of MO in water under UV or visible light irradiation was used as the illustrating example (**Figure 4**), where C was the absorption of MO at the wavelength of 465 nm and C_0 was the absorption after the adsorption equilibrium on the samples

Figure 3. Typical HRTEM images of (a) TiO_2 nanobelts, (b–e) CeO_2/TiO_2 (mole ratio 2:10) nanobelt heterostructures with different magnification and Fourier transform electron diffraction patterns of CeO_2.

and then the MO molecules can be degraded by UV or visible light. The UV-vis spectra (Figure S5) and total organic carbon (Figure S6) of methyl orange solutions after UV light irradiation using CeO_2/TiO_2 nanobelt heterostructure as photocatalyst also indicate that MO had been efficiently mineralized under UV light irradiation.

Further studies show that the photocatalytic activity of the CeO_2/TiO_2 nanobelt heterostructures also vary with the CeO_2/TiO_2 mole ratio, as depicted in panels (c) to (f). It can be seen that with increasing ratio of CeO_2/TiO_2, the photocatalytic activities of CeO_2/TiO_2 nanobelt heterostructures increase first, reach a maximum value at CeO_2/TiO_2 = 2:10, and then decrease (panels (c) to (f)). The possible reasons are proposed as follows. Under visible light irradiation, at a lower ratio of (1:10), the CeO_2/TiO_2 heterostructures can enhance the photocatalytic activity by promoting the separation of photogenerated holes and electrons, thus the visible photocatalytic activity of CeO_2/TiO_2 heterostructures is much higher than that of TiO_2 nanobelts. However, the visible photocatalysis property is still lower than that of pure CeO_2 nanoparticles; this is because the quantity of visible light photocatalyst CeO_2 nanoparticles is too low to absorb enough visible light. With the amount of CeO_2 increasing, the visible light active photocatalysis sites come from CeO_2 on TiO_2 nanobelts and the number of nanoheterostructures increase. When the mole ratio of CeO_2/TiO_2 reaches 2:10, a uniform layer of CeO_2 nanoparticles induce the maximum visible photocatalytic activity. This is about 23% higher than that of pure CeO_2 nanoparticles although the total amount of CeO_2 is less than 20% in the composite. Beyond this point, the photodegradation activity of CeO_2/TiO_2 nanobelt heterostructures decreases with increasing CeO_2/TiO_2 mole ratio. For instance, the activity becomes much lower than that of pure CeO_2 at the CeO_2/TiO_2 ratio of 4:10. This

may be caused by the agglomeration of CeO_2 nanoparticles (Figure S7), which blocked the transport and separation of photoinduced carriers. Moreover, the total amount of CeO_2 is still much lower than pure CeO_2 photocatalyst, and the decrease of effective CeO_2 active sites caused by the multilayer characteristics of CeO_2 on the TiO_2 nanobelt surface may be another reason for the reduction of the visible photocatalytic activity of the samples at higher CeO_2/TiO_2 ratios. For UV irradiation, when the CeO_2/TiO_2 mole ratio is as low as 1:10, the photocatalytic activity of the CeO_2/TiO_2 nanobelt composites is almost the same as that of TiO_2 nanobelts. When the CeO_2/TiO_2 mole ratio is 2:10, the photocatalysis property reaches the maximum value, i.e. the degradation percentage reaches almost 100% after 25 min degradation, which is about 40% higher than that of pure TiO_2 nanobelts, and 25% higher than that of P25 TiO_2 colloids. As mentioned above, CeO_2 is not a UV active photocatalyst, the enhanced UV photocatalysis activity of CeO_2/TiO_2 nanobelt composites should be contributed to the heterostructures. After reaching the maximum, the photocatalytic activity drops with a futher increase of the CeO_2/TiO_2 mole ratio. This may be caused by the UV light blocking effect of aggregated CeO_2 nanoparticles on the surface of TiO_2 nanobelts. When the CeO_2/TiO_2 mole ratio increases to 4:10, the UV photocatalytic activity is much lower than that of pure TiO_2 nanobelts. From the above discussion, we can conclude that the CeO_2/TiO_2 mole ratio influences the photocatalytic activity of the CeO_2/TiO_2 nanobelt composites, and the sample reaches the highest UV and visible photocatalytic activity at a CeO_2/TiO_2 mole ratio of 2:10.

To examine the photocatalytic stability of the catalysts, the efficiency of the photodegradation of MO was evaluated in a repetitive fashion with the same photocatalysts, and the results are shown in **Figure 5**. It can be seen that
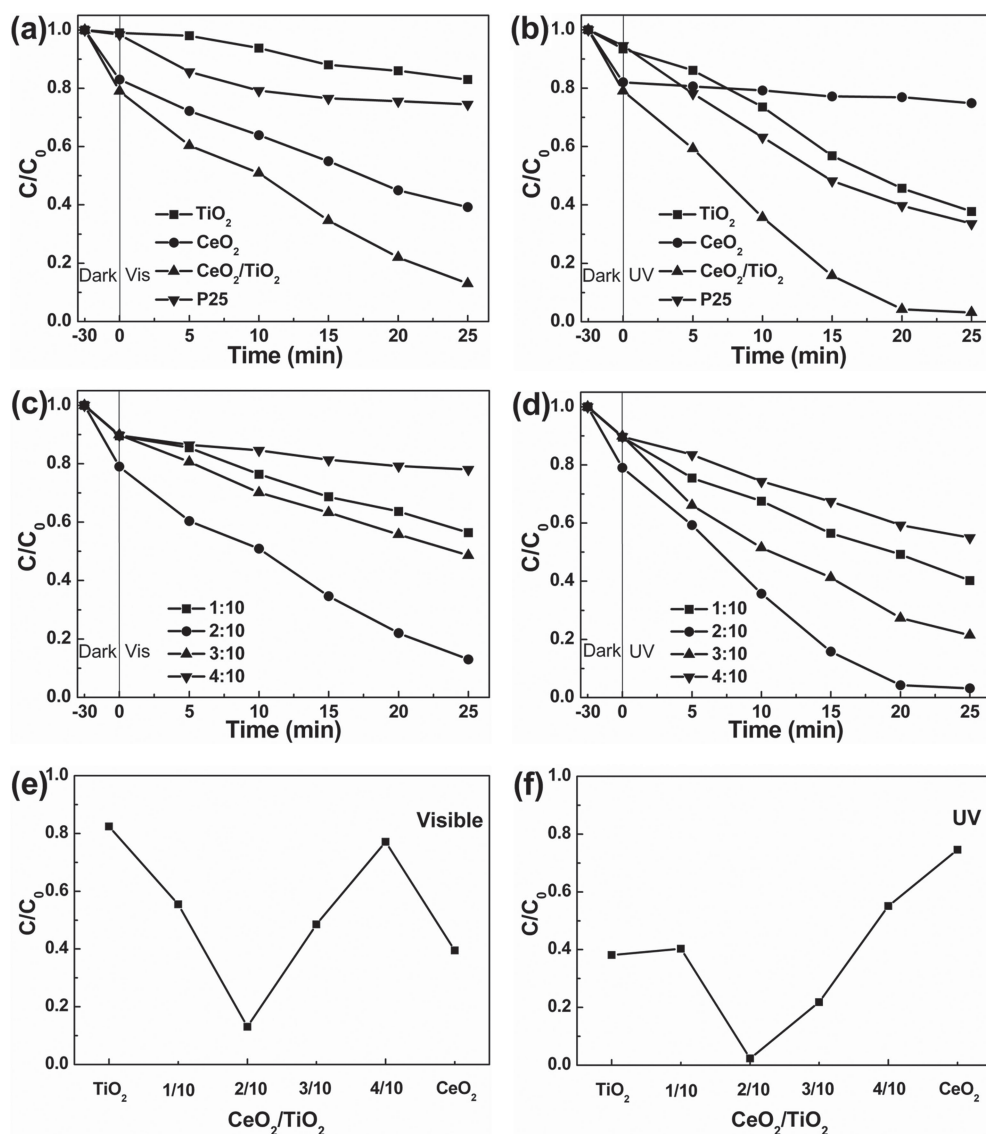
Figure 4. Photocatalytic degradation of MO in the presence of P25 TiO$_2$ colloids, TiO$_2$ nanobelts, CeO$_2$ nanoparticles and CeO$_2$/TiO$_2$ (mole ratio 2:10) nanobelt heterostructures under either (a) visible or (b) UV light irradiation. Comparison of the photocatalytic activities of the CeO$_2$/TiO$_2$ nanobelt heterostructures at different mole ratios of TiO$_2$ and CeO$_2$ under either (c) visible or (d) UV light irradiation. Variation of the fraction of MO that was photocatalytically degraded with CeO$_2$/TiO$_2$ heterostructures at different mole ratios of TiO$_2$ and CeO$_2$ after 25 min of irradiation of either (e) visible or (f) UV lights.

after four repetitive cycles the CeO$_2$/TiO$_2$ nanobelt heterostructures still maintain relatively consistent photocatalytic activity under either UV or visible light irradiation. For instance, after four repetitive cycles the remaining MO concentration only increased from <2% to 10% under UV irradiation, whereas under visible light irradiation, from 10% to 20%. However, the degradation decreases to 4% after four cycles' degradation in the dark (Figure S8). Without UV or visible light, only the capture of MO can occur in the MO solution, without the degradation process. With an increase of the times of repeated degradation, the MO capture will reach saturation on the heterostructure surface, and the capture effect of MO decreases quickly. However, under UV or visible light, as soon as MO molecules are captured by heterostructures, they are quickly photodegraded, and then

the degradation products are released to the solution. The whole process of degradation of the pollutant is based on a combined effect of capture–photodegradation–release. Thus, this heterostructure could work as an efficient and durable photocatalyst.

The Fourier-transform infrared (FTIR) spectra (**Figure 6**) were taken on the CeO$_2$/TiO$_2$ nanobelt heterostructures after absorption of MO in the dark for 30 min and then under visible light irradiation for 30 min to verify the capture–degradation–release catalysis process. The FTIR of MO (curve a) shows peaks corresponding to the asymmetric –CH$_3$ stretching vibrations at 2924.06 cm^{-1}, ring vibrations at 1036.7 cm^{-1}, and the –C–N band finger prints of the azo nature of dye at 1119.1 cm^{-1}. It is possible to distinguish wide absorption bands at 3458.82 cm^{-1} for the pure CeO$_2$/TiO$_2$
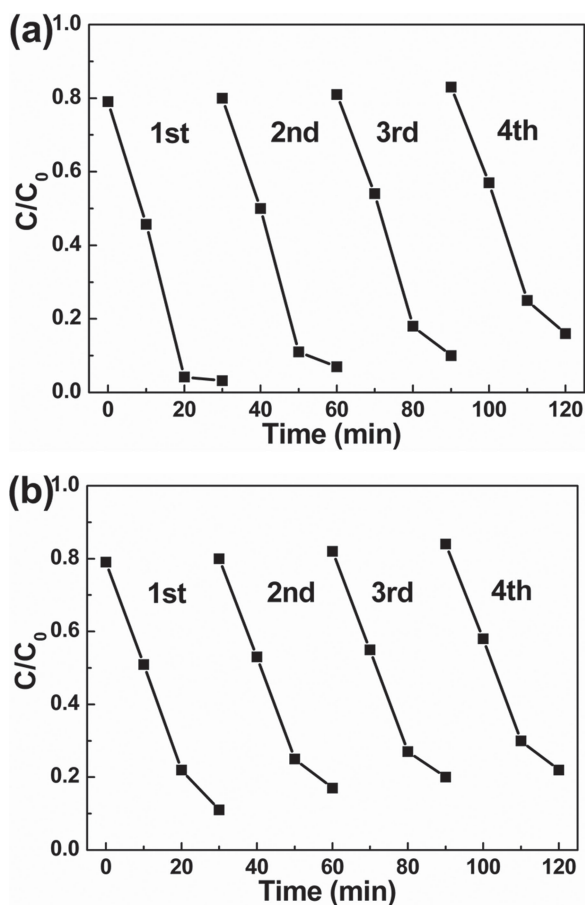
Figure 5. Photocatalytic degradation of MO by CeO_2/TiO_2 (mole ratio 2:10) nanobelt heterostructures in repeated experiments under (a) UV and (b) visible light irradiation.

Figure 6. FTIR spectra of (a) methyl orange, (b) CeO_2/TiO_2 nanobelt heterostructures, (c) CeO_2/TiO_2 nanobelt heterostructures after mixing with MO in the dark for 30 min, and (d) CeO_2/TiO_2 nanobelt heterostructures after mixing with MO in the dark for 30 min and then under visible light irradiation for 30 min.

nanobelt heterostructures (curve b), corresponding to the elongation mode of the -OH group.[17] The peaks at 1632.94, 1558.65 and 1414.34 cm^{-1} were also due to the banding of hydroxyl groups.[18] After the composite catalyst is kept in MO in the dark for 30 min (curve c), the typical IR vibration peaks of MO at 1118.6 and 1035.59 cm^{-1} can be found in the spectrum of the CeO_2/TiO_2 nanobelt heterostructures samples, which confirms that the capture of methyl orange occurs. After photocatalytic degradation of MO under UV light irradiation (curve d), the peaks of CeO_2/TiO_2 nanobelt heterostructures can be found, and no peaks corresponding to MO retains, which suggests a complete degradation of MO. This observation offers powerful evidence for the capture-photodegradation-release mechanism performed by the CeO_2/TiO_2 nanobelt heterostructures during the MO degradation process.

The observed photocatalytic activity of the CeO_2/TiO_2 heterostructures is consistent with the optical absorption characteristics. **Figure 7** shows the UV-vis diffuse reflectance spectrum (DRS) of TiO_2 nanobelts, CeO_2 nanoparticles, and CeO_2/TiO_2 nanobelt heterostructures. It can be seen that the TiO_2 nanobelts exhibit a steep absorption edge located at 380 nm (curve a), consistent with the large bandgaps.[8a] In contrast, CeO_2 nanoparticles display obvious absorption up
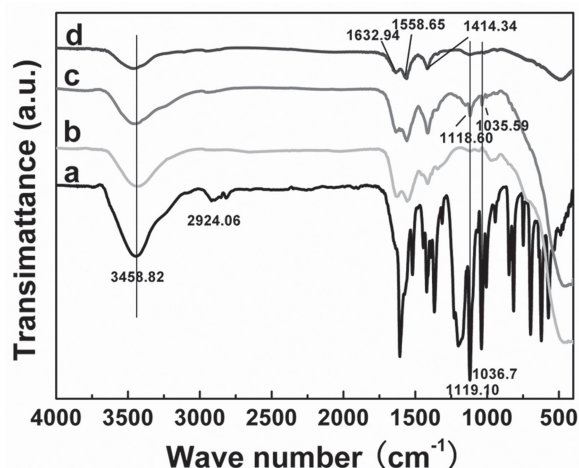
to 500 nm (curve b). CeO_2/TiO_2 nanobelt heterostructures also exhibit a similar absorption profile in the UV to visible range (300 to 700 nm) (curve c). This indicates that the photodegradation application might cover the UV and visible light range. For the CeO_2/TiO_2 nanobelt heterostructure, visible light can be absorbed by CeO_2 nanoparticles on the surface of TiO_2 nanobelts, and UV light can pass through the CeO_2 nanoparticles or the blank areas on the surface of TiO_2 nanobelts, and harvested by TiO_2 nanobelts. The absorption edge of TiO_2 nanobelts, CeO_2 nanoparticles, and CeO_2/TiO_2 nanobelt heterostructures is determined to be 393 nm, 456 nm, and 495 nm, respectively, according to Figure 7. Therefore, their respective bandgap energy is evaluated to be 3.15 eV, 2.72 eV, and 2.51 eV.

Photoluminescence spectra are usually used to explore the efficiency of the charge carrier trapping, migration, and transfer, and it is quite helpful to understand the fate of electron-hole pairs in semiconductor particles as PL emission arises from the recombination of free carriers.[19] **Figure 8** shows the PL spectra of the TiO_2 nanobelts, CeO_2 nanoparticles and CeO_2/TiO_2 nanobelt heterostructures. The excitation wavelength was set at 300 nm. TiO_2 nanobelts exhibited two strong emission peaks at around 400 nm and 470 nm, which might be attributed to the emission of the bandgap transition and that of the charge transfer transition of oxygen vacancy trapped electrons,[20] respectively. The CeO_2 nanoparticles showed a strong emission peak at around 460 nm, which is attributed to the intrinsic luminescence of CeO_2. An obvious decrease of the photoluminescence of the CeO_2/TiO_2 nanobelt heterostructures was observed as compared with that of TiO_2 nanobelts or CeO_2 nanoparticles alone, indicating that the coupling of TiO_2 and CeO_2 in the heterostructures effectively diminished the recombination of photoinduced electron-hole pairs, which was beneficial to the photocatalytic activity.

The enhanced photocatalytic activity of the CeO_2/TiO_2 nanobelt heterostructures under either UV or visible

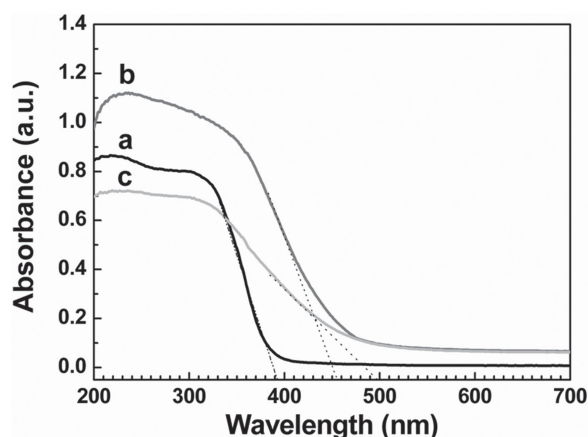**Figure 7.** UV-vis diffuse reflectance spectra of (a) TiO_2 nanobelts, (b) CeO_2 nanoparticles and (c) CeO_2/TiO_2 (mole ratio 2:10) nanobelt heterostructures.
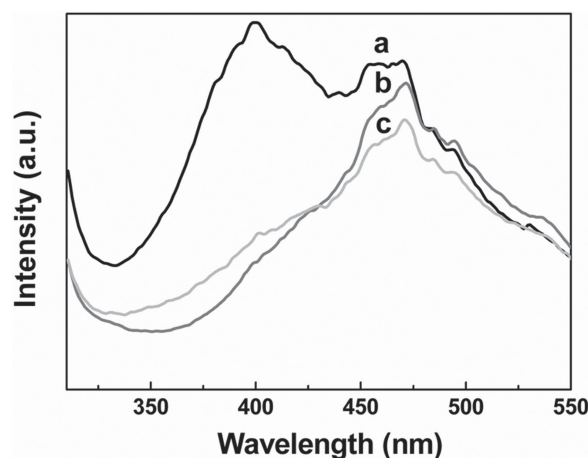

Figure 8. Photoluminescence (PL) spectra of (a) TiO_2 nanobelts, (b) CeO_2 nanoparticles and (c) CeO_2/TiO_2 (mole ratio 2:10) nanobelt heterostructures, $\lambda_{Ex} = 300$ nm.

irradiation may be accounted for by the following factors. First, the CeO_2 nanoparticles on TiO_2 nanobelts forming the heterostructures possess visible light and UV light activity, and the heterostructures with an appropriate CeO_2 nanoparticle distribution can combine both UV and visible photocatalysis properties. Second, heterostructures with matched band structures inhibit recombination of photo-generated electron-hole pairs, which is the main reason of the enhancement of the photocatalytic activity of the CeO_2/TiO_2 nanobelt heterostructures.[21] As discussed above (Figure 8), the heterostructures realize the inhibition of the recombination of photoinduced electron-hole pairs. And this allows more photogenerated electrons to participate in the reduction reaction to form superoxide radicals (O_2^+), a strong oxidant which can degrade MO effectively. The photogenerated holes participate in the oxidation reaction to produce hydroxyl radicals (-OH), which is a very strong oxidant to favor the degradation of organic substances simultaneously. Third, as mentioned above, CeO_2/TiO_2 nanobelt heterostructures have a strong capture ability of MO, which endows the photocatalyst a novel capture effect to collect the MO molecules to the surface of catalyst and promote the photodegradation efficiency. Based on the above discussion, the photodegradation process likely involves three steps: MO capture, degradation, and release, the so-called capture-degradation-release mechanism as illustrated in **Figure 9**.

Typically, the MO is captured by the CeO_2 nanoparticles on the surface of heterostructure, then quickly photodegraded under UV or visible light irradiation, and ultimately the degradation products are released to the external environment. Note that the conduction and valence band positions can be determined by using the following empirical equation:[22]

$$E_{CB} = X - E_e - 0.5E_g \qquad (1)$$

where E_{CB} denotes the conduction band edge potential, X the geometric mean of the Mulliken electronegativity of the constituent atoms, E_e the energy of free electrons on the

hydrogen scale (about 4.5 eV) and E_g is the bandgap. The X values for TiO_2 and CeO_2 are about 5.81 eV and 5.56 eV, respectively,[23] and the corresponding E_g values are 3.15 eV and 2.72 eV. Thus, the positions of the conduction band edge (E_{CB}) at the point of zero charge are estimated to be –0.27 eV and –0.3 eV, respectively.

There will be two typical modes of photocatalysis in CeO_2/TiO_2 nanobelt heterostructures under UV and visible light irradiation. Firstly, when exposed to UV light, both TiO_2 and CeO_2 can be excited, which results in the creation of photogenerated holes in the valence band (VB) and electrons in their conduction band (CB). CB electrons (CeO_2) easily migrate to the CB of TiO_2 through the interface, because the conduction band-edge potential of CeO_2 (–0.3 eV) is more negative than that of TiO_2 (–0.27 eV). Similarly, because the valence band-edge potential of CeO_2 (2.42 eV) is lower than that of TiO_2 (2.88 eV), VB holes (TiO_2) can inject to the VB of CeO_2 by the control of the interface. It is more helpful for the separation of photoinduced electron-hole pairs in TiO_2 and CeO_2, resulting in the improvement of photocatalysis under UV irradiation. On the other hand, in the visible light region, the electrons in the VB CeO_2 are excited to its CB under irradiation. CeO_2 would be excited by the visible light and generate electron-hole pairs. The photogenerated electrons in the CB of CeO_2 can be transferred to the CB of TiO_2, leading to efficient charge separation.[24]

3. Conclusion

CeO_2/TiO_2 nanobelt heterostructures have been prepared by an economic and practical hydrothermal method. Both UV and visible photocatalytic activities of CeO_2/TiO_2 nanobelt heterostructures are greatly enhanced compared to TiO_2 nanobelts and CeO_2 nanoparticles. For CeO_2/TiO_2 nanobelt heterostructures, the excellent photocatalysis process can be divided to three steps, capture of MO molecules on the surface of CeO_2, photodegradation of MO molecules, and release of the degraded molecules, the so called
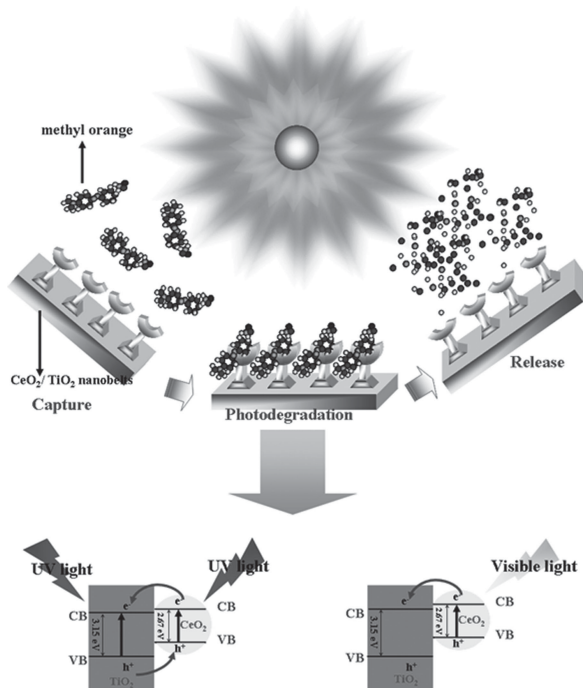
Figure 9. Schematic of the capture–photodegradation–release mechanism of methyl orange degradation by CeO$_2$/TiO$_2$ nanobelt heterostructures under UV and visible light irradiation.

capture–photodegradation–release mechanism. The optimal CeO$_2$/TiO$_2$ ratio of CeO$_2$/TiO$_2$ nanobelt heterostructures is 2:10. The enhanced broad light wavelength region photocatalytic activities of CeO$_2$/TiO$_2$ nanobelt heterostructures are ascribed to four reasons: 1) Combination with both CeO$_2$ nanoparticles and TiO$_2$ nanobelts causes broad light wavelength absorption; 2) large surface area of CeO$_2$ nanoparticles causes large amount visible light absorption without sheltering UV light; 3) energy band matching between CeO$_2$ nanoparticles and TiO$_2$ nanobelts causes the separation of photoinduced electron-hole pairs; 4) higher surface area of CeO$_2$ nanoparticles on the surface of TiO$_2$ nanobelts caused strong capture of MO molecules. The concept of capture of the pollutant followed by photocatalytic degradation and release should be open a new approach for design and synthesis of high performance photocatalysts.

4. Experimental Section

Materials: The chemicals used in this work were of analytical reagent grade. Solutions were freshly prepared with deionized water. Titania P25 (TiO$_2$; ca. 80% anatase, and 20% rutile), sodium hydroxide (NaOH), hydrochloric acid (HCl), sulfuric acid (H$_2$SO$_4$), ammonium hydroxide(NH$_3$·H$_2$O; 25–28%) and cerium nitrate dihydrate (Ce(NO$_3$)$_3$·2H$_2$O) were purchased from Sinopharm and used without further treatment.

Preparation of TiO$_2$ Nanobelts: TiO$_2$ nanobelts were synthesized by a hydrothermal procedure.[6] Typically, P25 powders (0.1 g) was mixed with an aqueous solution of NaOH (20 mL, 10 mol/L), followed by a hydrothermal treatment at 180 °C in a 25 mL Teflon-lined

autoclave for 48 h. The treated powders were washed thoroughly with deionized water followed by a filtration and drying process. The obtained sodium titanate nanobelts were then immersed in an aqueous solution of HCl (0.1 mol/L) for 48 h and then washed thoroughly with water to produce H$_2$Ti$_3$O$_7$ nanobelts. The H$_2$Ti$_3$O$_7$ nanobelts were added into a 25 mL Teflon vessel, which was filled with an aqueous solution of H$_2$SO$_4$ (0.02 mol/L) up to 80% of the total volume and maintained at 100 °C for 12 h. Finally, the products were isolated from the solution by centrifugation and sequentially washed with deionized water for several times, and dried at 70 °C for 10 h. Thermal annealing of the H$_2$Ti$_3$O$_7$ nanobelts by acid corrosion at 600 °C for 2 h led to the production of TiO$_2$ nanobelts with roughened surfaces.

Preparation of CeO$_2$/TiO$_2$ Nanobelt Heterostructures: CeO$_2$/TiO$_2$ nanobelt heterostructures at various mole ratios from 1:10 to 4:10 were prepared by a simple hydrothermal co-precipitation method. In a typical reaction, Ce(NO$_3$)$_3$·2H$_2$O (0.15–0.6 mmol) and TiO$_2$ nanobelts (1.5 mmol) prepared above were dispersed in 100 mL of deionized water. After vigorous stirring for 30 min, ammonium hydroxide was dropped into the solution to adjust the pH to 9–10. The suspension was then heated at 100 °C for 48 h. By washing with deionized water and ethanol, the dried powders were calcined in air at 550 °C for 2 h to prepare CeO$_2$/TiO$_2$ nanobelt heterostructures. For comparison, CeO$_2$ nanoparticles were also prepared in a similar fashion.

Materials Characterization: X-ray powder diffraction (XRD) patterns of the heterostructures were recorded on a Bruke D8 Advance powder X-ray diffractometer with Cu Kα (λ = 0.15406 nm). A HITACHI S-4800 field emission scanning electron microscope (FE-SEM) was used to characterize the morphology of the synthesized samples, and the chemical composition was examined via energy-dispersive X-ray spectroscopy (EDS) attached to the FE-SEM. High resolution transmission electron microscopic (HRTEM) images were acquired with a JOEL JEM 2100 microscope. Fourier-transform infrared (FTIR) spectra were collected on a Nicolet Avatar 370 infrared spectrometer in the range of 400–4000 cm^{-1} using pressed KBr discs. The KBr pellets were prepared where 10 mg of a sample was mixed with 1000 mg of KBr in an agate mortar. From this stock, 200 mg were then pressed into pellets of 13 mm in diameter. UV–vis diffuse reflectance spectra (DRS) of the samples were recorded on a UV–vis spectrophotometer (UV-2550, Shimadzu) with an integrating sphere attachment within the range of 200 to 700 nm and with BaSO$_4$ as the reflectance standard. The photoluminescence (PL) spectra were acquired at room temperature with a FLS920 fluorescence spectrometer under the ultraviolet excitation of 300 nm. Total organic carbon of the MO solution was analyzed with the total organic carbon analyzer (Shimadzu TOC V-CPH). X-ray photoelectron spectroscopy (XPS) was performed using an ESCALAB 250. The specific surface area was calculated using the Brunauer–Emmett–Teller (BET) method using the measurement instrument (Micromeritics, ASAP2020).

Photocatalytic Test: The photocatalytic activity of the CeO$_2$/TiO$_2$ nanobelt heterostructures was investigated by the photodegradation of methyl orange (MO, 20 mg/L). In a typical measurement, 20 mL of an aqueous suspension of MO and 20 mg of the heterostructure powders were placed in a 50 mL beaker. Prior to photoirradiation, the suspensions were magnetically stirred in the dark for 30 min to establish adsorption-desorption equilibrium

between the dye and the surface of the catalysts under ambient conditions. A 350 W mercury lamp with a maximum emission at 356 nm was used as the UV source, and a 300 W Xe arc lamp (wave length > 410 nm by pass filter) as the visible light source for visible light photocatalysis. At varied irradiation time intervals, an aliquot of the mixed solution was collected and centrifuged, and the residual MO concentration in the supernatant was analyzed by UV–vis spectroscopic measurements (Hitachi UV-3100).

[1] a) S. Iijima, *Nature* **1991**, *354*, 56–58; b) I. Paramasivam, H. Jha, N. Liu, P. Schmuki, *Small* **2012**, *8*, 3073–3103; c) N. Q. Wu, J. Wang, D. N. Tafen, H. Wang, J. G. Zheng, J. P. Lewis, X. G. Liu, S. S. Leonard, A. Manivannan, *J. Am. Chem. Soc.* **2010**, *132*, 6679–6685.

[2] a) Y. M. Wang, G. J. Du, H. Liu, D. Liu, S. B. Qin, N. Wang, C. G. Hu, X. T. Tao, J. Jiao, J. Y. Wang, Z. L. Wang, *Adv. Funct. Mater.* **2008**, *18*, 1131–1137; b) J. K. Yuan, X. G. Liu, O. Akbulut, J. Q. Hu, S. L. Suib, J. Kong, F. Stellacci, *Nat. Nanotechnol.* **2008**, *3*, 332–336; c) J. Wang, D. N. Tafen, J. P. Lewis, Z. L. Hong, A. Manivannan, M. J. Zhi, M. Li, N. Q. Wu, *J. Am. Chem. Soc.* **2009**, *131*, 12290–12297; d) I. Paramasivam, A. Avhale, A. Inayat, A. Bösmann, P. Schmuki, W. Schwieger, *Nanotechnology* **2009**, *20*, 225607–225611.

[3] a) Z. Xiong, X. Zhao, *J. Am. Chem. Soc.* **2012**, *134*, 5754–5757; b) Y. C. Chen, Y. C. Pu, Y. J. Hsu, *J. Phys. Chem. C* **2012**, *116*, 2967–2975.

[4] a) W. J. Zhou, H. Liu, R. I. Boughton, G. J. Du, J. J. Lin, J. Y. Wang, D. Liu, *J. Mater. Chem.* **2010**, *20*, 5993–6008; b) X. B. Chen, S. S. Mao, *Chem. Rev.* **2007**, *107*, 2891–2959.

[5] H. Zhang, D. Chen, X. J. Lv, Y. Wang, H. X. Chang, J. H. Li, *Chem. Mater.* **2008**, *20*, 6543–6549.

[6] W. J. Zhou, X. Y. Liu, J. J. Cui, D. Liu, J. Li, H. D. Jiang, J. Y. Wang, H. Liu, *CrystEngComm* **2011**, *13*, 4557–4563.

[7] a) R. Y. Liu, P. G. Hu, S. W. Chen, *Appl. Surf. Sci.* **2012**, *258*, 9805–9809; b) T. D. Nguyen, C. T. Dinh, T. O. Do, *Nanoscale* **2011**, *3*, 1861–1873.

[8] a) W. J. Zhou, G. J. Du, P. G. Hu, G. H. Li, D. Z. Wang, H. Liu, J. Y. Wang, R. I. Boughton, D. Liu, H. D. Jiang, *J. Mater. Chem.* **2011**, *21*, 7937–7945; b) J. J. Lin, J. X. Shen, R. J. Wang, J. J. Cui, W. J. Zhou, P. G. Hu, D. Liu, H. Liu, J. Y. Wang, R. I. Boughton, Y. Z. Yue, *J. Mater. Chem.* **2011**, *21*, 5106–5113.

[9] Z. R. Tang, Y. H. Zhang, Y. J. Xu, *RSC Adv.* **2011**, *1*, 1772–1777.

[10] a) M. D. Hernandez-Alonso, F. Fresno, S. Suarez, J. M. Coronado, *Energy Environ. Sci.* **2009**, *2*, 1231–1257; b) A. Bruix, J. A. Rodriguez, P. J. Ramírez, S. D. Senanayake, J. Evans, J. B. Park, D. Stacchiola, P. Liu, J. Hrbek, F. Illas, *J. Am. Chem. Soc.* **2012**, *134*, 8968–8974.

[11] P. Borker, A. V. Salker, *Mater. Chem. Phys.* **2007**, *103*, 366–370.

[12] a) S. Kundu, J. Ciston, S. D. Senanayake, D. A. Arena, E. Fujita, D. Stacchiola, L. Barrio, R. M. Navarro, J. L. G. Fierro, J. A. Rodriguez, *J. Phys. Chem. C* **2012**, *116*, 14062–14070; b) I. Alessandri, M. Zucca, M. Ferroni, E. Bontempi, L. E. Depero, *Small* **2009**, *5*, 336–340; c) B. T. Jiang, S. Y. Zhang, X. Z. Guo, B. K. Jin, Y. P. Tian, *Appl. Surf. Sci.* **2009**, *255*, 5975–5978.

[13] G. S. Li, D. Q. Zhang, J. C. Yu, *Phys. Chem. Chem. Phys.* **2009**, *11*, 3775–3782.

[14] S. M. Meybodia, S. A. Hosseinib, M. Rezaeec, S. K. Sadrnezhaadd, D. Mohammadyanib, *Ultrason. Sonochem.* **2012**, *19*, 841–845.

[15] A. Nilchi, M. Yaftian, G. Aboulhasanlo, S. Rasouli Garmarodi, *J. Radioanal. Nucl. Chem.* **2009**, *279*, 65–74.

[16] D. C. Sayle, X. D. Feng, Y. Ding, Z. L. Wang, T. X. T. Sayle, *Cryst. Growth Des.* **2011**, *11*, 4129–4134.

[17] Q. Fang, B. Chen, *Carbon* **2012**, *50*, 2209–2219.

[18] a) J. T. Last, *Phys. Rev.* **1957**, *105*, 1740–1750; b) S. Tursiloadi, H. Imai, H. Hirashima, *J. Non-Cryst. Solids* **2004**, *350*, 271–276; c) Z. Li, B. Hou, Y. Xu, D. Wu, Y. Sun, W. Hu, F. Deng, *J. Solid State Chem.* **2005**, *178*, 1395–1405.

[19] F. B. Li, X. Z. Li, *Chemosphere* **2002**, *48*, 1103–1111.

[20] Y. Lei, L. D. Zhang, G. W. Meng, G. H. Li, X. Y. Zhang, C. H. Liang, W. Chen, S. X. Wang, *Appl. Phys. Lett.* **2001**, *78*, 1125–1127.

[21] a) Y. Y. Li, J. P. Liu, X. T. Huang, J. G. Yu, *Dalton Trans.* **2010**, *39*, 3420–3425; b) K. L. Lv, J. G. Yu, K. J. Deng, X. H. Li, M. Li, *J. Phys. Chem. Solid* **2010**, *71*, 519–522.

[22] A. H. Nethercot Jr., *Phys. Rev. Lett.* **1974**, *33*, 1088–1091.

[23] a) Y. Xu, M. A. A. Schoonen, *Am. Mineral.* **2000**, *85*, 543–556; b) G. Magesh, B. Viswanathan, R. P. Viswanath, T. K. Varadarajan, *Indian J. Chem.* **2009**, *48A*, 480–488.

[24] G. R. Bamwenda, T. Uesigi, Y. Abe, K. Sayama, H. Arakawa, *Appl. Catal. A* **2001**, *205*, 117–128.